TED Plaza

Ways To Watch Drops Dry

Yutaku Kita

King's College London, Lecturer
Department of Engineering
yutaku.kita@kcl.ac.uk

1. Introduction

Drops (or droplets if they are very small) are common in nature and have intrigued the giants in science such as Thomas Young, Pierre-Simon Laplace and James Clark Maxwell over the centuries. Drops have become important in engineering and technology since the 1980s, when inkjet printing, coating and nanopatterning technologies emerged. Therefore, evaporation and flows in drops on a substrate, i.e., sessile drops, have attracted a lot of research interest.

Experimental studies of drop evaporation started from measuring the mass change, i.e., evaporation rate, using a mass balance (Morse, 1910). To date, video recording of drop evaporation is more popular as it can provide more information such as drop shape, e.g., radius and contact angles, and the triple-phase contact line dynamics.

One may that watching a drop evaporate is boring, as it seems to be a simple process; however, drop systems involve complex interactions of hydrodynamics, heat and mass transfer and wetting phenomena at different scales. We can certainly appreciate the beauty of the complex phenomena using suitable techniques. For instance, particle image velocimetry (PIV) has been widely used to study flow structures inside drops under various conditions (Christy et al., 2011; Hamamoto et al., 2011; Hu & Larson, 2006). Interferometry can visualise the vapour distributions around drops and study the diffusion process and the effect of external flows (Dehaeck et al., 2014). Infrared (IR) thermal cameras have been a powerful tool to obtain temperature fields within liquids. As a drop evaporates, which is an endothermic process, temperature distributions are formed across the drop, driving convective flows and affecting vapour pressure distributions at the liquid-vapour interface. Therefore, it is crucial to systematically understand temperature, flow and vapour fields of drops under phase change using appropriate measurement techniques.

I have been working on phase change of sessile drops for several years using some of the techniques mentioned above. In the present article, I will share some of my experiences with IR thermography and the background-oriented schlieren (BOS) technique for drop research including some successful (meaning published) and not-so-successful (meaning not published "yet") cases.

2. Infrared Thermography for Drops

IR thermography enables temperature measurement for liquids without disturbing the flow. Savino and Fico (Savino & Fico, 2004) were among the first to report thermographs of evaporating hanging drops, revealing the effect of Marangoni convection on the temperature distributions. Moreover, IR thermography has identified some intriguing phenomena on evaporating sessile drops such as hydrothermal waves (HTWs), which are self-excited instabilities due to the Marangoni effect (Sefiane et al., 2008). Despite the successful applications of IR thermography for the drop research, the analysis of their IR data remained qualitative. The difficulty of IR imaging of liquids originates in the partial transparency of the fluids to the wavelengths used for the camera. That is, the temperature read by the camera is affected by the energy emitted, transmitted and reflected by the drop and the surroundings, not just by the liquid temperature. In

this section, I will show how to interpret IR data properly by considering all possible radiation sources and optical properties.

2.1 Effect of ambient temperature and relative humidity on HTWs probed by IR thermography

Fig. 1 represents our experimental setup. The motivation of this work was to investigate how ambient conditions affect HTWs and the evaporation of ethanol drops. An approximately 7 µL of ethanol was gently deposited onto a polished copper substrate coated with a 20 nm thick CYTOP (from AGC) layer. We used an IR camera (FLIR SC4000MW) for the top view and a CCD camera (Sentech STC0MC152USB) for the side view. We varied the ambient temperature (T_{amb} = 10 °C – 40 °C) and the relative humidity of water vapour (RH = 25% – 90%) in an environmental chamber (ESPEC PR-3KT).

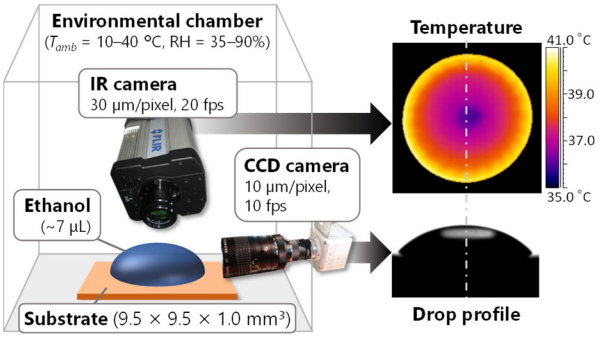

Fig. 1 Experimental setup for infrared imaging of evaporating ethanol drops under controlled environmental conditions.

Fig. 2 shows raw thermographs for T_{amb} = 40 °C, RH = 35% and 90%. The dark regions outside the drop are not the actual temperature of the substrate. They were caused by the reflection of the cold emission from the IR sensor, which was cooled by the Stirling cooler. The polished copper surface has high IR reflectivity (ca. 0.9), and therefore, IR cameras cannot measure its temperature accurately. This is generally a tricky nature of IR thermography; however, it also makes the drop distinguishable from the substrate, which helps with image processing.

As the evaporation sets in, the drop becomes colder than the substrate, which transfers heat to the substrate to the drop and the liquid-vapour interface. As the centre of the drop has a longer heat conduction path than the edges, the temperature decreases towards the apex, resulting in the temperature distribution shown in Fig. 2. For RH = 35%, we observed an azimuthal wavy temperature pattern, which corresponds to HTWs driven by the temperature gradient along the liquid-vapour interface from the edge to the apex. The temperature of the entire drop decreased as the evaporation proceeded, resulting in the reduced wave number. For higher RH, on the other hand, the HTWs were irregular from the early stage of evaporation, and the drop temperature remained higher than the low RH cases. These influences of RH on the temperature and HTWs imply some interactions between the moisture and the drop at the interface. Since similar trends were observed for other T_{amb} conditions, I will only present the results for T_{amb} = 40 °C here.

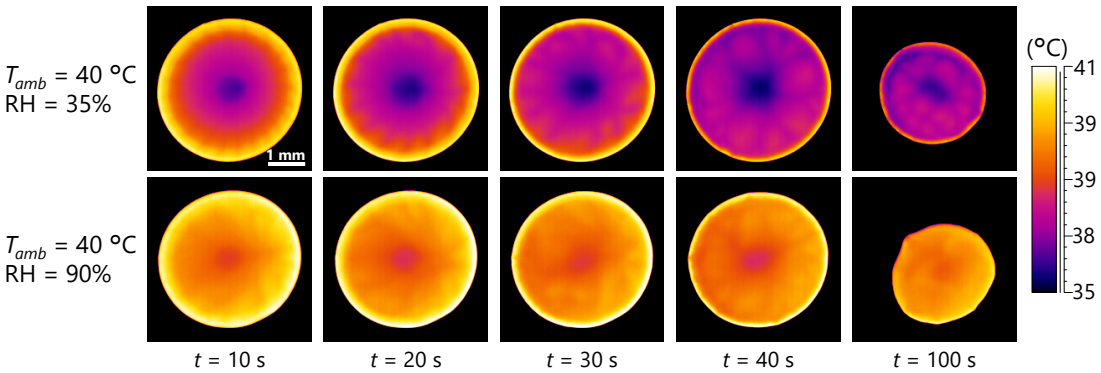

Fig. 2 Raw thermal images for T_{amb} = 40 °C and RH = 30% (top) and 90% (bottom).

2.2 Calculation of temperature at the liquid-vapour interface

The raw IR data in Fig. 2 do not represent the surface temperature or mean temperature of the drop and are only for qualitative comparison and description. The temperature indicated T_c is affected by T_{amb} and the substrate temperature T_w in addition to the liquid temperature T_l (Fig. 3 (a)). This is because the camera receives the radiation energies from the drop, the surroundings and the substrate, denoted as E_l (T_l), E_{amb} (T_{amb}) and E_w (T_w), respectively. The total energy the IR camera receives E_c (T_c) can be expressed as

$$E_c(T_c) = \varepsilon_{app}E_l(T_l) + \rho_{app}E_{amb}(T_{amb}) + \tau_{app}E_w(T_w), \tag{1}$$

where ε_{app}, ρ_{app} and τ_{app} are the apparent emissivity, reflectivity and transmissivity of the drop, respectively. Since the temperature across the drop is not uniform, the radiant energy emitted at each location within the drop must be considered. The radiant energies emitted from an arbitrary height (z) to the liquid vapour interface ($z = h$) and to the substrate surface ($z = 0$) follow the Beer-Lambert law. Integrating each energy from $z = 0$ to $z = h$ gives the total energy in each direction, $E_{l\text{-}v}$ and $E_{l\text{-}w}$, namely

$$E_{l-v}[T_l(z)] = \int_0^h \kappa_l E_{b,\lambda_1-\lambda_2}[T_l(z)]e^{-\kappa_l(h-z)}dz, \tag{2}$$

$$E_{l-w}[T_l(z)] = \int_0^h \kappa_l E_{b,\lambda_1-\lambda_2}[T_l(z)]e^{-\kappa_l z}dz, \tag{3}$$

where κ_l is the absorption coefficient of the liquid (κ_l = 1850 m^{-1} for ethanol), and $E_{b,\lambda_1-\lambda_2}$ is the energy of black body radiation within the range of wavelengths used for the camera, which depends on temperature by Planck's law. These radiant energies are repeatedly reflected at the liquid-vapour and solid-liquid interfaces, transmitted (with absorption) through the liquid and reach the camera sensor. Finally, the energy that approaches from the drop to the camera is

$$\varepsilon_{app}E_l = \varepsilon_{app,l-v}E_{l-v} + \varepsilon_{app,l-w}E_{l-w}, \tag{4}$$

where

$$\varepsilon_{app,l-v} = (1-\rho_{lv})/(1-\tau_l^2\rho_{lv}\rho_{lw}), \tag{5}$$

$$\varepsilon_{app,l-w} = (1-\rho_{lv})\tau_l\rho_{lw}/(1-\tau_l^2\rho_{lv}\rho_{lw}). \tag{6}$$

Here, the reflectivity of the liquid-vapour interface ρ_{lv} can be calculated using the refractive indices of air (n_{air} = 1) and ethanol (n_l = 1.36) as $\rho_{lv} = [(n_l - n_{air})/(n_l + n_{air})]^2 = 0.0233$. The reflectivity of the solid-liquid interface was assumed to be ρ_{sl} = 0.9, which was identical to the reflectivity of polished copper surface. The transmissivity of the liquid τ_l varies with the liquid thickness (or the drop height) h and can be expressed as $\tau_l = e^{-\kappa_l h}$. The height h at each location was obtained by the side-view image taken with the CCD camera.

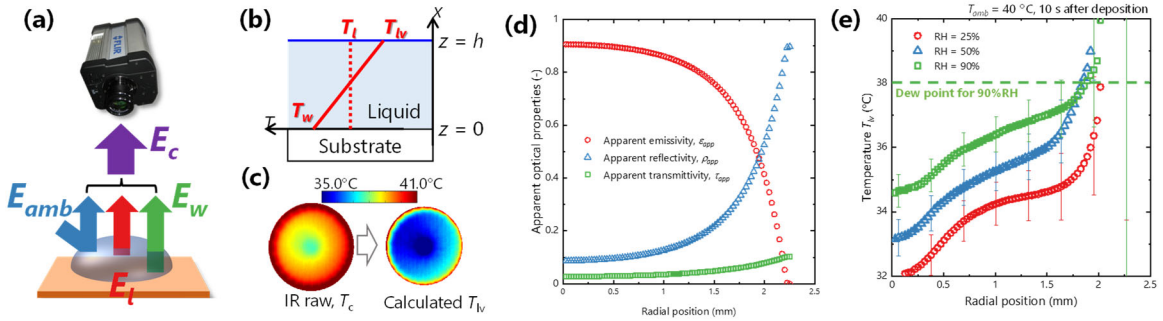

Fig. 3 (a) Sources of radiant energy captured by the IR camera. (b) Assumed temperature distributions within the drop. Two extreme cases are considered i.e., a linear temperature distribution (solid line) and a uniform temperature distribution (dotted line). (c) Raw and processed (with the linear temperature distribution approximation) temperature maps of the drop. (d) Radial distribution of the apparent optical properties values. (e) T_{lv} as a function of radial position for different RH.

Radiation from the surroundings and the substrate can be treated similarly. First, E_{amb} and E_w can be calculated as $\varepsilon_{amb}E_{b,\lambda_1-\lambda_2}(T_{amb})$ and $\varepsilon_w E_{b,\lambda_1-\lambda_2}(T_w)$, respectively. Here, ε_{amb} and ε_w are the emissivities of the surroundings and the substrate, respectively, and were assumed to be ε_{amb} = 1.0 and ε_w = 0.1. These radiations also reach to the camera after reflection at the interfaces and absorption within the liquid. Hence, ρ_{app} and τ_{app} can be expressed as

$$\rho_{app} = \rho_{lv} + (1-\rho_{lv})^2\tau_l^2\rho_{lw}/(1-\tau_l^2\rho_{lv}\rho_{lw}), \quad (7)$$

$$\tau_{app} = (1-\rho_{lv})\tau_l/(1-\tau_l^2\rho_{lv}\rho_{lw}). \quad (8)$$

Combining Eqs. (1)–(8), the temperature profile within the liquid $T_l(z)$ is the only unknown variable. The surface temperature of the drop T_{lv} can be determined by making an appropriate assumption of $T_l(z)$. However, it is nearly impossible to measure or predict $T_l(z)$ accurately. Therefore, we considered two extreme cases (see Fig. 3 (b)): (i) conduction dominant (linear temperature), i.e., $T_l(z) = T_w + mz$, where m is the slope. (ii) completely mixed (uniform temperature), i.e., $T_l(z) = T_l$. In calculations, we numerically determined m (for the case (i)) or T_l (for the case (ii)) that satisfied Eq. (1). Although the true value of T_{lv} should exist between the values calculated for those two cases, in this article, I will only discuss the case (i). Fig. 3 (c) presents an example of processed thermographs. Calculated T_{lv} was significantly lower than the raw temperature T_c. This is reasonable as the effect of radiations from the surroundings and substrate, which remained warmer than the drop, has been taken into account. Now, it should be noted that the uncertainty of T_{lv} becomes larger near the contact line as the liquid becomes thinner, resulting in more significant effect of the external radiations relative to the one from the drop itself. Since ε_{app}, ρ_{app} and τ_{app} depend on h, their values change drastically along the radial position, and at some point ρ_{app} becomes larger than ε_{app}, leading to a significant error (see Fig. 3 (d)). Detailed descriptions of the data processing can be found in our published work (Fukatani et al., 2016).

Fig. 3 (e) plots radial distributions of azimuthally averaged T_{lv} at 10 seconds after deposition. The temperature at the drop surface was significantly lower than the dew point under higher RH conditions e.g., RH = 90% as represented by the dashed line in the figure. This implies possible condensation of the surrounding water vapour at the liquid-vapour interface during ethanol evaporation. Later, we confirmed adsorption-absorption and/or condensation of water using Gas Chromatography (Kita et al., 2018). The heat released by the water intake maintained the drop surface temperature higher at higher RH as observed in Fig. 2. The disturbed HTWs could be attributed to both the non-uniform heat release of and the local water-ethanol concentration change which may have caused the solutal Marangoni effect.

3. Vapour Phase Visualisation for Drops

Let us now focus on the vapour phase surrounding the drop. The vapour is saturated near the liquid-vapour interface and diffuses towards the atmosphere where its concentration is lower, driving evaporation. Based on this theory, diffusion-limited models have been proposed to predict the rate of drop evaporation (Hu & Larson, 2002; Picknett & Bexon, 1977; Popov, 2005; Schofield et al., 2018). In addition, natural convection has been reported to play a role in evaporation of fluids with different vapour densities than air (Kelly-Zion et al., 2011). While these theoretical and computational analysis have provided insight into vapour distributions their effect on the evaporation, conventional experiments only measured global evaporation rates until Dehaeck et al. used Mach-Zehnder interferometry (MZI) to quantify local evaporative flux (Dehaeck et al., 2014). MZI is used to detect changes in the refractive index of fluids n which depends on the density ρ i.e.,

$$n = K\rho + 1, \quad (9)$$

where K is the Gladstone-Dale constant. Despite its success in the literature, MZI has some complexities in the setup (e.g., coherent light sources such as lasers and highly accurate positioning of optical components) and image processing.

3.1 Principle of the background-oriented schlieren technique

Here, we propose the Background-Oriented Schlieren (BOS) technique as an alternative approach to vapour field visualisation. This is a more recently developed technique (Dalziel et al., 2000) and has been used in aerospace engineering, combustions and gas/underwater shock waves. One main advantage of the BOS technique over conventional interferometry is the simplicity of optical equipment and image processing. As illustrated in Fig. 4, the minimum components required for this technique are a background

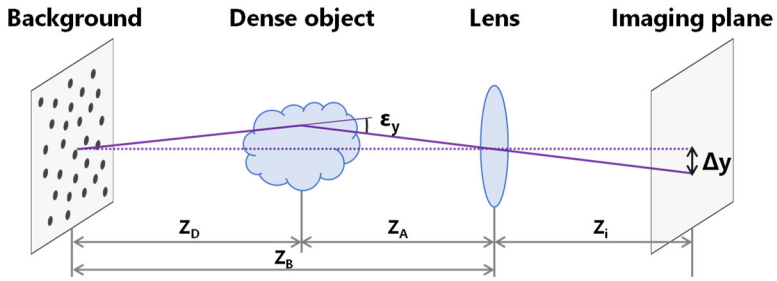

Fig. 4 Basic configuration of BOS imaging technique.

and an imaging device e.g., a camera with a lens, and the dense phase object (i.e., evaporating drops) should be placed between them. As the background light refracts as it passes through the dense phase object, distorting of the background. A reference background image without the dense phase object may be recorded in advance and compared to the distorted one. Using the image correlation methods, which are commonly used for PIV, the distortion of the background can be quantified as the displacement Δy. Under the paraxial approximation i.e., for small deflection angles ($\varepsilon_y \approx \tan \varepsilon_y$), Δy can be expressed as

$$\Delta y = Z_D M \varepsilon_y, \tag{10}$$

where $M = Z_i/Z_B$ is the magnification factor in which Z_i and Z_B are the distances between the imaging plane (i.e., camera sensor) and the lens and the lens and the background, respectively. Z_D is the distance between the dense phase object and the background. The deflection angle ε_y can be directly related to the refractive index gradient as

$$\varepsilon_y = \frac{1}{n_0} \int \frac{\partial n}{\partial y} dz, \tag{11}$$

where n_0 is the refractive index of the reference atmosphere (i.e., air). Combining Eqs. (10) and (11) allows to relate the background displacements to the gradient of refractive index.

3.2 Material selection

The small size of the drops being investigated limits the choice of fluids to ensure measurable distortion of the background. In other words, fluids must have a sufficiently large contrast of the refractive indices between the pure vapour and the ambient gas. Therefore, liquids such as water and ethanol are not suitable for this technique. As this limitation applies to MZI as well, Dehaeck et al. used HFE-7000 with the refractive index of ca. 1.00163 (Dehaeck et al., 2014). In the present study, we used acetone which has a similarly high refractive index of 1.001090 (*Refractive Index Common Liquids, Solids and Gases*, 2008).

3.3 BOS setup

Fig. 5 shows the schematic of our experimental setup for BOS imaging. As the background, a random dot pattern was printed on a transparent plastic film and backlit by a collimated white LED light. The collimated light enables a longer depth of field such that the distance between the background and the object can be maximised to obtain a larger image displacement due to density variation. A silicon wafer coated with CYTOP was used as the substrate and located approximately 100 mm away from the background. A CMOS camera was then located approximately 140 mm away from the location at which acetone was deposited and focused on the background. Despite the light being collimated, the edges of the drop recorded by the camera were blurred due to the distance between the background and the drop (see Fig. 5). Therefore, a beam splitter was added to the setup, after the substrate, and an additional camera is located to focus on the drops (see Fig. 5). We started recording both cameras before depositing the drops (ca. 6 μL) so that we captured frames without drops as the reference image of the background.

3.4 Results

Here, I present some of our first trial results and discuss them only qualitatively. We processed the images to quantify the distortion of the background dots using a cross-correlation algorithm, which is commonly used for PIV. Among open source and commercial software and codes, we used PIVlab on

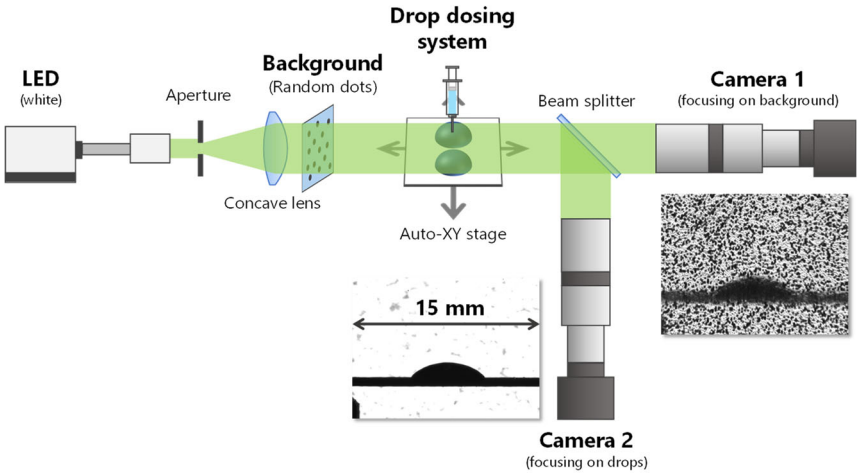

Fig. 5 Schematic of the current BOS setup.

Matlab to process the images. Fig. 6 (a) depicts the total displacement profiles, which directly correspond to the refractive index and density gradient (i.e., vapour concentration) profile around the acetone drop. The images represent the projection of the refractive index gradients through the vapour cloud, and appropriate topological reconstruction e.g., inverse Abel transform is required. However, in this article, we only present unprocessed data and keep the discussion qualitative. We found wide regions of large distortion above the drop and steep gradients of displacement near the contact line, which implies high evaporative fluxes. This agrees well qualitatively with analytical solutions and numerical simulations in literature (Dunn et al., 2008; Pan et al., 2014).

We are particularly interested in evaporation of multiple drops. While abundant studies have focused on single drop evaporation, recent studies have revealed a strong effect of the existence of neighbouring drops (Hegde et al., 2018; Kobayashi et al., 2010; Schofield et al., 2020; Wray et al., 2020, 2021). This is primarily due to the vapour concentration profile deviating from the single drop scenario. We therefore attempted to experimentally visualise the vapour field around a pair of evaporating drops. Fig. 6 (b) shows the displacement profile for a pair of drops with an edge-to-edge distance of ca. 1 mm. In agreement with the analytical solution, the vapour was more concentrated in the space between the drops, resulting in slower evaporation i.e., shielding effect (Schofield et al., 2020).

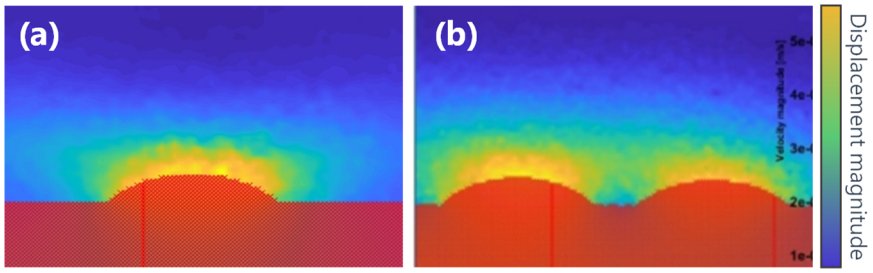

Fig. 6 Colourmap of displacement of the background image for (a) a single drop and (b) a drop pair.

4. Summary and Conclusion

Novel techniques emerge year by year, enabling us to advance our knowledge of multiphase flows in various systems. In this article, I described two techniques to study evaporating sessile drops, namely, IR thermography and BOS. IR thermography offers valuable information of thermal activities and their implications for flow motion; however, we need to interpret the camera data appropriately to enable quantitative investigations. Detailed procedures to calculate the surface temperature of an IR semi-transparent drops have been described in this article. I have also introduced the BOS technique for evaporating drops. Although still under development, our preliminary results showed great potential in understanding vapour transfer around drops in various configurations.

Acknowledgements

This work was partly supported by the EC-RISE-ThermaSMART project. This project has received funding from the European Union's Horizon 2020 research and innovation programme under the Marie Skłodowska-Curie grant agreement No. 778104.

References

Christy, J. R. E., Hamamoto, Y., & Sefiane, K. (2011). Flow transition within an evaporating binary mixture sessile drop. Physical Review Letters, 106(20), 1–4. https://doi.org/10.1103/PhysRevLett.106.205701

Dalziel, S. B., Hughes, G. O., & Sutherland, B. R. (2000). Whole-field density measurements by "synthetic schlieren." Experiments in Fluids, 28(4), 322–335. https://doi.org/10.1007/s003480050391

Dehaeck, S., Rednikov, A., & Colinet, P. (2014). Vapor-Based Interferometric Measurement of Local Evaporation Rate and Interfacial Temperature of Evaporating Droplets. Langmuir, 30(8), 2002–2008. https://doi.org/10.1021/la404999z

Dunn, G. J., Wilson, S. K., Duffy, B. R., David, S., & Sefiane, K. (2008). A mathematical model for the evaporation of a thin sessile liquid droplet: Comparison between experiment and theory. Colloids and Surfaces A: Physicochemical and Engineering Aspects, 323(1–3), 50–55. https://doi.org/10.1016/j.colsurfa.2007.09.031

Fukatani, Y., Orejon, D., Kita, Y., Takata, Y., Kim, J., & Sefiane, K. (2016). Effect of ambient temperature and relative humidity on interfacial temperature during early stages of drop evaporation. Physical Review E, 93(4), 043103. https://doi.org/10.1103/PhysRevE.93.043103

Hamamoto, Y., Christy, J. R. E., & Sefiane, K. (2011). Order-of-magnitude increase in flow velocity driven by mass conservation during the evaporation of sessile drops. Physical Review E - Statistical, Nonlinear, and Soft Matter Physics, 83(5), 1–5. https://doi.org/10.1103/PhysRevE.83.051602

Hegde, O., Chakraborty, S., Kabi, P., & Basu, S. (2018). Vapor mediated control of microscale flow in sessile droplets. Physics of Fluids, 30(12), 122103. https://doi.org/10.1063/1.5054632

Hu, H., & Larson, R. G. (2002). Evaporation of a sessile droplet on a substrate. Journal of Physical Chemistry B, 106(6), 1334–1344. https://doi.org/10.1021/jp0118322

Hu, H., & Larson, R. G. (2006). Marangoni effect reverses coffee-ring depositions. Journal of Physical Chemistry B, 110(14), 7090–7094. https://doi.org/10.1021/jp0609232

Kelly-Zion, P. L., Pursell, C. J., Vaidya, S., & Batra, J. (2011). Evaporation of sessile drops under combined diffusion and natural convection. Colloids and Surfaces A: Physicochemical and Engineering Aspects, 381(1–3), 31–36. https://doi.org/10.1016/j.colsurfa.2011.03.020

Kita, Y., Okauchi, Y., Fukatani, Y., Orejon, D., Kohno, M., Takata, Y., & Sefiane, K. (2018). Quantifying vapor transfer into evaporating ethanol drops in a humid atmosphere. Physical Chemistry Chemical Physics, 20(29), 19430–19440. https://doi.org/10.1039/C8CP02521E

Kobayashi, M., Makino, M., Okuzono, T., & Doi, M. (2010). Interference effects in the drying of polymer droplets on substrate. Journal of the Physical Society of Japan, 79(4). https://doi.org/10.1143/JPSJ.79.044802

Morse, H. W. (1910). On Evaporation from the Surface of a Solid Sphere. Preliminary Note. Proceedings of the American Academy of Arts and Sciences, 45(14), 363. https://doi.org/10.2307/20022561

Pan, Z., Weibel, J., & Garimella, S. (2014). Influence of Surface Wettability on Transport Mechanisms Governing Water Droplet Evaporation. Langmuir, 30(2), 9726–9730. https://doi.org/10.1021/la501931x

Picknett, R. G., & Bexon, R. (1977). The evaporation of sessile or pendant drops in still air. Journal of Colloid and Interface Science, 61(2), 336–350. https://doi.org/10.1016/0021-9797(77)90396-4

Popov, Y. O. (2005). Evaporative deposition patterns: Spatial dimensions of the deposit. Physical Review E, 71(3), 036313. https://doi.org/10.1103/PhysRevE.71.036313

Refractive Index common Liquids, Solids and Gases. (2008). https://www.engineeringtoolbox.com/refractive-index-d_1264.html

Savino, R., & Fico, S. (2004). Transient Marangoni convection in hanging evaporating drops. Physics of Fluids, 16(10), 3738–3754. https://doi.org/10.1063/1.1772380

Schofield, F. G. H., Wilson, S. K., Pritchard, D., & Sefiane, K. (2018). The lifetimes of evaporating sessile droplets are significantly extended by strong thermal effects. Journal of Fluid Mechanics, 851, 231–244. https://doi.org/10.1017/jfm.2018.496

Schofield, F. G. H., Wray, A. W., Pritchard, D., & Wilson, S. K. (2020). The shielding effect extends the lifetimes of two-dimensional sessile droplets. Journal of Engineering Mathematics, 120(1), 89–110. https://doi.org/10.1007/s10665-019-10033-7

Sefiane, K., Moffat, J. R., Matar, O. K., & Craster, R. V. (2008). Self-excited hydrothermal waves in evaporating sessile drops. Applied Physics Letters, 93(7), 074103. https://doi.org/10.1063/1.2969072

Wray, A. W., Duffy, B. R., & Wilson, S. K. (2020). Competitive evaporation of multiple sessile droplets. Journal of Fluid Mechanics, 884, A45. https://doi.org/10.1017/jfm.2019.919

Wray, A. W., Wray, P. S., Duffy, B. R., & Wilson, S. K. (2021). Contact-line deposits from multiple evaporating droplets. Physical Review Fluids, 6(7). https://doi.org/10.1103/PhysRevFluids.6.073604